PHYSICAL REVIEW B **96**, 205423 (2017)

Nature of carrier injection in metal/2D-semiconductor interface and its implications for the limits of contact resistance

Divya Somvanshi,[1,*] Sangeeth Kallatt,[1,2] Chenniappan Venkatesh,[1] Smitha Nair,[2] Garima Gupta,[1] John Kiran Anthony,[3] Debjani Karmakar,[4] and Kausik Majumdar[1,†]

[1]*Department of Electrical Communication Engineering, Indian Institute of Science, Bangalore 560012, India*
[2]*Center for Nano Science and Engineering, Indian Institute of Science, Bangalore 560012, India*
[3]*Renishaw India, Bangalore 560011, India*
[4]*Technical Physics Division, Bhabha Atomic Research Centre, Trombay, Mumbai 400085, India*

(Received 26 February 2017; revised manuscript received 23 October 2017; published 15 November 2017)

Monolayers of transition metal dichalcogenides (TMDCs) exhibit excellent electronic and optical properties. However, the performance of these two-dimensional (2D) devices are often limited by the large resistance offered by the metal contact interface. To date, the carrier injection mechanism from metal to 2D TMDC layers remains unclear, with widely varying reports of Schottky barrier height (SBH) and contact resistance (R_c), particularly in the monolayer limit. In this paper, we use a combination of theory and experiments in Au and Ni contacted monolayer MoS_2 device to elucidate the following points: (i) the carriers are injected at the source contact through a cascade of two potential barriers—the barrier heights being determined by the degree of interaction between the metal and the TMDC layer; (ii) the conventional Richardson equation becomes invalid due to the multidimensional nature of the injection barriers, and using Bardeen-Tersoff theory, we derive the appropriate form of the Richardson equation that describes such a composite barrier; (iii) we propose a novel transfer length method (TLM) based SBH extraction methodology, to reliably extract SBH by eliminating any confounding effect of temperature dependent channel resistance variation; (iv) we derive the Landauer limit of the contact resistance achievable in such devices. A comparison of the limits with the experimentally achieved contact resistance reveals plenty of room for technological improvements.

DOI: 10.1103/PhysRevB.96.205423

I. INTRODUCTION

Two-dimensional (2D) transition metal dichalcogenides (TMDCs) are promising materials for novel electronic and optoelectronic device applications [1,2]. Monolayer and few layers of these materials have been shown to be very promising for light generation [3,4] and detection [5,6] applications. On the other hand, the ability to suppress surface roughness scattering at subnanometer thickness, coupled with an appreciable band gap, makes them promising candidates to enable logic transistor scaling beyond 10 nm [7]. However, the performance of most of these electronic and optoelectronic devices are bottlenecked by a relatively large parasitic contact resistance [8–11]. On the contrary, in photodetection applications, the metal/TMDC interface plays active role in enhancing photoresponse [12,13]. Thus, it is important to understand the nature of the interface between the metal and the TMDC in these devices. However, despite its importance, there has been a limited effort to understand the origin of the intrinsic mechanisms that control the characteristics of this interface.

The Schottky barrier height (SBH) and the contact resistance of a metal/TMDC interface have been reported in the past [14–25], however, with a large spread, particularly at the monolayer limit [8,26–30]. In this paper, we use a combination of *ab initio* theory, systematic experiments, and modeling to reveal the underlying mechanisms that control the SBH and the contact resistance. With the help of *ab initio* calculation and material characterization, we first study the modification of electronic properties of monolayer MoS_2 underneath the metal contact due to metal induced charge transfer. Next, we propose a two-barrier carrier injection model arising from this charge transfer between the contact metal and 2D material underneath. We then derive the corresponding modified Richardson equation of this composite barrier based on Bardeen-Tersoff theory. The magnitude of the effective potential barrier is obtained experimentally by using a novel transfer length method (TLM) based extraction methodology and is found to be a strong function of device operating condition. This extraction method carefully excludes any ambiguity resulting from channel resistance variation due to temperature. Further insights into the mechanism is obtained by validating the experimental results with solution of one-dimensional (1D) coupled Poisson-Schrödinger (CPS) equations. Finally, the Landauer limit [31] of the contact resistance achievable in such a structure is derived analytically and compared with the experimental results. All the results described below are based on Au and Ni contacted monolayer MoS_2 devices, but the conclusions remain qualitatively valid for a generic top contacted layered semiconductor interface, if the thickness of the semiconductor remains close to the 2D limit.

II. NATURE OF CARRIER INJECTION AT SOURCE JUNCTION

Figure 1 shows the schematic diagram of a monolayer MoS_2 film on SiO_2/Si substrate and contacted by a metal pad from the top. Along the channel direction, such a contact, in general, has been treated like a conventional metal-semiconductor

*Present address: Department of Electronics and Telecommunication Engineering, Jadavpur University, Kolkata 700032, India.
†Corresponding author: kausikm@iisc.ac.in

 ©2017 American Physical Society

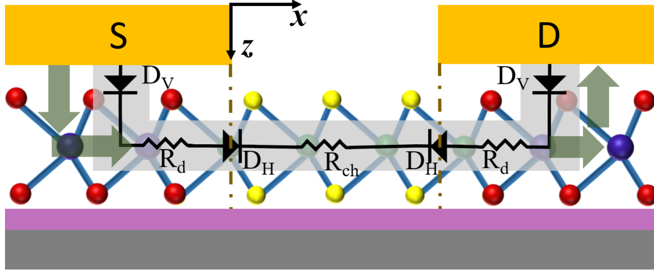

FIG. 1. Schematic diagram showing possible carrier injection process from metal to monolayer MoS_2. This is modeled as a series connection of back-to-back diodes and resistor in a backgated device. The arrows indicate the direction of electron flow (opposite of current flow).

band bending [14] with strong Fermi level pinning and tunneling induced field emission. However, note that there is no provision for band bending vertically downward in the ultrathin sandwich layer. This forces the carrier injection mechanism as a cascade of multiple processes [30,32], as schematically shown in Fig. 1: (i) the vertically downward injection of carriers to the thin film underneath the metal, where the 2D film is modified electronically due to proximity of metal; (ii) horizontal transport of carriers through the modified 2D film underneath the metal contact (the current crowding regime); and (iii) horizontal injection of carriers to the channel over a second barrier arising from the doping difference between the 2D films under the metal contact and the 2D film in the channel. Consequently, such a cascaded carrier injection process can be modeled as a series combination of two diodes and a resistor at the source end. Before going into the details of the carrier injection mechanism through the cascaded processes, we first discuss the properties of the monolayer MoS_2 film underneath the metal contact.

III. MODIFIED ELECTRONIC PROPERTIES OF MONOLAYER MoS_2 IN PROXIMITY OF METAL

Clearly, the 2D film underneath the contact plays the mediating role between the source and the channel in the carrier injection process. Former *ab initio* calculations have been performed to study interfaces between TMDC monolayers and metal surfaces [33–36]. We use *ab initio* calculations to obtain insight into the charge transfer between metal (Au or Ni) and monolayer MoS_2. As sulfur vacancies (SV) are considered as one of the most probable defects in MoS_2, we consider both with and without SV cases. This is followed by optical and electrical characterization of monolayer MoS_2 film in the proximity of metal.

A. *Ab initio* calculation details

The MoS_2/Au interface is constructed by combining the $4 \times 4 \times 1$ monolayer of Au [111] surface on the $4 \times 4 \times 1$ monolayer of 1H-MoS_2. Due to the mismatch in the lattice parameters of Au [111] and 1H-MoS_2, there is an initial lateral strain of ~9.7% on the Au layer, which after structural relaxation, turns out to be 6.08%. In a similar procedure, keeping a minimal lattice parameter incongruity, MoS_2/Ni interface is built by combining a $5 \times 5 \times 1$ monolayer of Ni [111] surface on the $4 \times 4 \times 1$ monolayer of 1H-MoS_2 with 1.5% initial lateral strain on Ni-layer, which after structural relaxation remains almost the same. To avoid replication from the z-directional periodicity, a vacuum of 10 Å was added both above and below the constructed interface. These interfaces are also investigated in the presence of ~6% SV, known to be the most common defect to occur in 1H-MoS_2. Thus, we investigate four such interfaces, *viz.* Au, Au + SV, Ni, and Ni + SV with 1H-MoS_2. To resemble the realistic experimental scenario, we have also investigated the interfaces of monolayer MoS_2 and bilayer metals.

These interfaces were explored with the help of *ab initio* density functional theory (DFT) based formalism using a plane wave pseudopotential approach with projector-augmented wave (PAW) potentials, as implemented in the Vienna *Ab initio* Simulation Package (VASP). Electron correlation within the system is treated using Perdew-Burke-Ernzerhof exchange-correlation functional under the spin-polarized generalized gradient approximation (GGA). Ionic and lattice parameter optimization of the constructed interfaces are obtained by a conjugate gradient algorithm until the Hellmann-Feynman forces on each ion is less than 0.01 eV/Å. To account for the interface-induced dipolar interaction, we have incorporated the van der Waals corrections by using Grimme DFT-D2 method [37]. In this method, a semiempirical dispersion potential is added to the conventional density functional energy after taking care of intersurface interactions. For self-consistent calculations and structure optimization, an energy cutoff of 500 eV is used with a k-point mesh size $5 \times 5 \times 3$.

B. *Ab initio* results

The layer (LPDOS) and orbital (OPDOS) projected density of states are summarized in Figs. 2(a)–2(e), and the corresponding charge densities are shown in Figs. 2(f)–2(i). Covalent charge sharing between Ni and S is more favorable than Au, as Au has a relatively more closed shell structure, while Ni has a partially filled valence $3d$ orbital. We have started with a distance of 3.2 Å between both of the layers for all four cases. After relaxation, the average distance between Au and 1H-MoS_2 becomes ~3 Å. The value for Ni turns out to be ~2.2 Å. The average distance reduces to 2.8 and 2.0 Å for Au + SV and Ni + SV cases, respectively, implying proximity of the metal layer to 1H-MoS_2 in the presence of SV.

In monolayer MoS_2, the π-bonded S-p_x, p_y and Mo-$d_{xy}, d_{x2\text{-}y2}$ and $d_{3z2\text{-}1}$ orbitals populate the states at the top of the valence band and bottom of the conduction band in the bonding and antibonding manifold respectively. The Au layer, having a filled $5d$ orbital and delocalized $6s$ electrons, transfers its $6s$ electrons to the Mo-$4d$ orbitals via S-$3p_x$ and $3p_y$. A close observation of Fig. 2(b) unveils that the Au-S hybridized bonding orbitals populate energy states from −1.5 to −3 eV, which are filled Au-$5d$ states. The charge transfer from Au-$6s$ to S or Mo renders a delocalization of Au-$6s$ electrons. The states from −1.5 to −0.4 eV are having more Mo-$4d$ and S-$3p$ bonding characters than Au-$6s$, implying the already occurred charge transfer from Au layer to MoS_2. These transferred electrons fill up the Mo-d_{xy}, $d_{x2\text{-}y2}$, and $d_{3z2\text{-}1}$

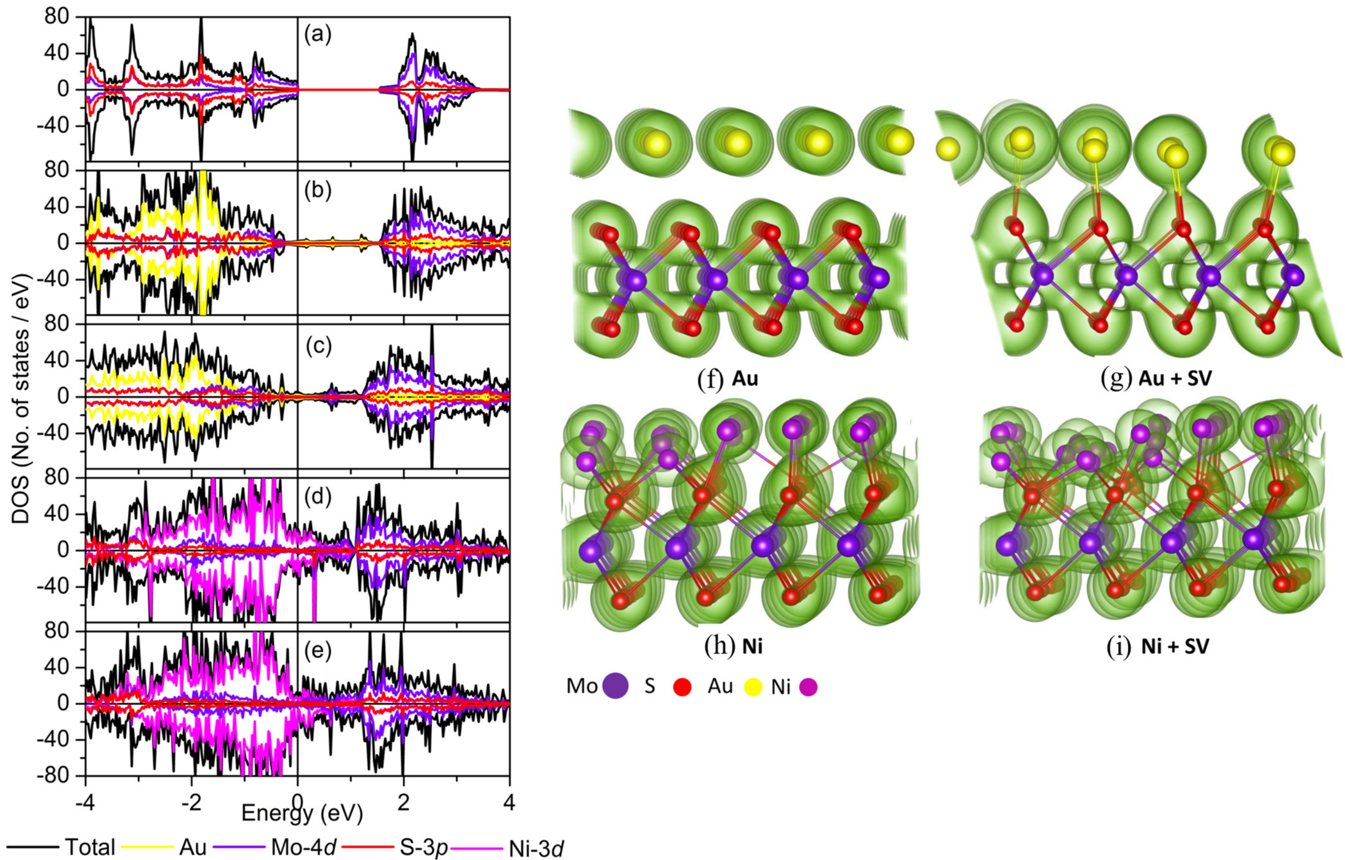

FIG. 2. Electronic structure of monolayer MoS_2 under monolayer metal. (a) The LPDOS and OPDOS for (a) pristine 1H-MoS_2, (b) Au/MoS_2 interface, (c) Au/MoS_2 interface with interfacial SV, (d) Ni/MoS_2 interface, (e) Ni/MoS_2 interface with interfacial SV. (f) Charge density plots for Au/MoS_2 interface, (g) Au/MoS_2 interface with interfacial SV, (h) Ni/MoS_2 interface, and (i) Ni/MoS_2 interface with interfacial SV.

orbitals and thereby shifts the E_F toward the conduction band. Due to such a complete charge transfer, the probability of formation of gold sulphide is less. In the presence of SV, the shift of E_F is more, as the absence of S-3p orbital allows the direct charge transfer from Au-6s to Mo-4d, implying an increase in the extent of n-type doping. Bader analysis for charge transfer has revealed that for Au and Au + SV cases, there is an average charge transfer of 0.8e and 1.5e per atom respectively from Au to the MoS_2 layer. This interfacial charge is calculated after integrating the charge over a volume around the interface between two specific z values. The lesser amount of charge at the Au/MoS_2 interface (than Ni/MoS_2 interface as discussed later) and more localized charge distribution at the individual layer suggests tunnelling nature of charge transfer for Au/MoS_2 contacts [38].

The presence of partially filled 3d orbitals makes Ni a better contact for MoS_2. The Ni/MoS_2 interface, both with and without SV, exhibits metallic property [Figs. 2(d) and 2(e)] with a strong Fermi level shift toward the conduction band, due to the covalent nature of the charge transfer from Ni-3d to S-3p and formation of nearly compensated antiferromagnetic metal nickel sulphides at the interface. Contrary to Au, for Ni, S-3p DOS is highly delocalized and hybridizes with Ni-3d OPDOS. The amount of charge transfer from the Ni to MoS_2 layer is 0.5e and 1.2e for Ni and Ni+SV cases, respectively. The interfacial charge for Ni interface is ~4 times higher than the Au-interface. This result can be visualized from the charge density plots presented in Figs. 2(h) and 2(i), indicating a much higher charge overlap and bonding of Ni and S ions.

As a next-step, we have investigated the impact of increasing the thickness of the metal layer by constructing interfaces of the MoS_2 monolayer and metal bilayer. The OPDOS for these systems are depicted in Figs. 3(a) and 3(b). The corresponding charge density plots are presented in Figs. 3(c) and 3(d), respectively. For the MoS_2/Au interface, increment of metal-layer thickness leads to more delocalized Au-6s states in an energy range of −1 to +1 eV around E_F, mainly having contributions from the top Au layer. The delocalized electrons from the layer adjacent to MoS_2 have already transferred the n-type carriers to the beneath MoS_2 layer. Due to the nonspin polarized nature of 6s electrons, the system remains nonmagnetic irrespective of increase of Au-layer thickness, as is evident from Fig. 3(a). Interface with Ni, on the contrary, has a strong impact on the spin polarization of the system. The Ni layer adjacent to MoS_2 forms antiferromagnetic nickel sulphide at the interface, leading to the partial DOS of Ni-3d electrons almost same at E_F for both spin-up and spin-down states. With the increasing thickness of the Ni layer, the ferromagnetic nature of bulk Ni prevails over the interfacial antiferromagnetic nature, resulting into more spin polarization at E_F. This trend becomes obvious from Fig. 3(b). The spin-polarized Ni-3d states near E_F is less hybridized with

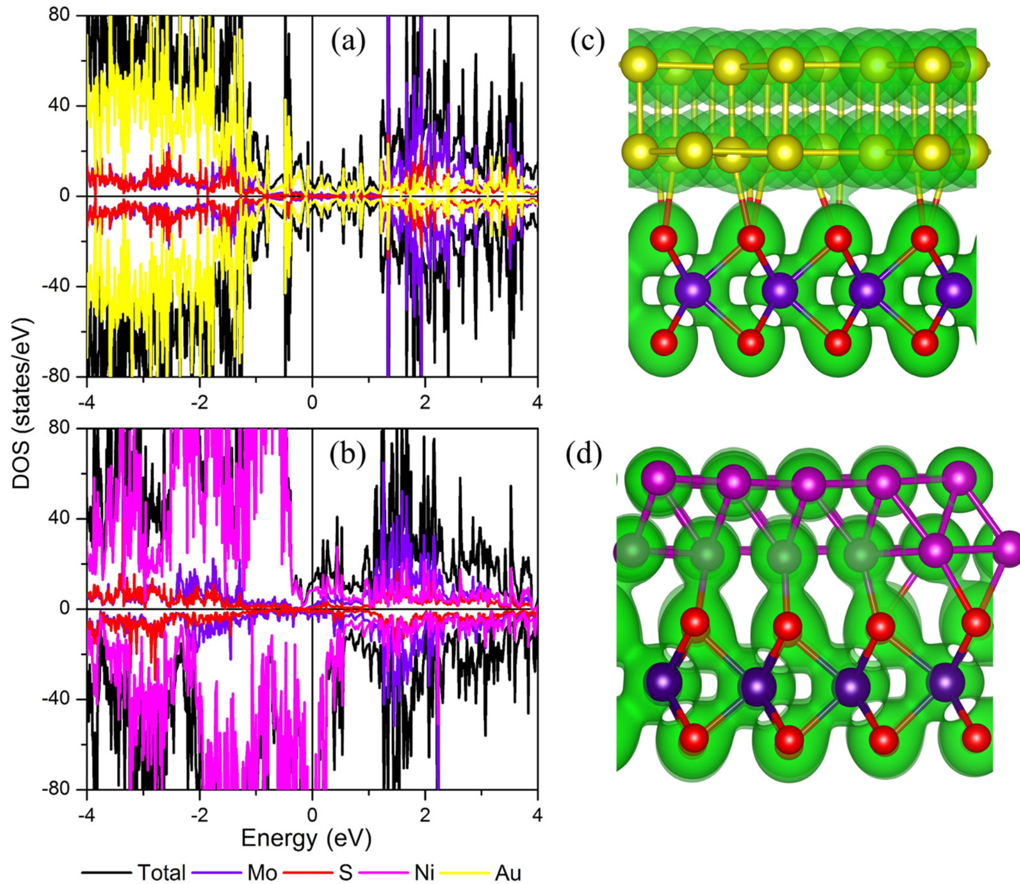

FIG. 3. Electronic structure of monolayer MoS_2 under bilayer metal. (a) Monolayer-MoS_2/bilayer-Au DOS, (b) monolayer-MoS_2/bilayer-Ni DOS, (c) MoS_2/Au charge density plot, (d) MoS_2/Ni charge density plot.

S-3p states, implying lesser covalent nature of additional Ni layer with S. Nature of charge transfer is similar to the monolayer metal cases, as can be seen from Figs. 3(c) and 3(d), since the adjacent layer contributes the most in charge transfer. Interfacial charge remains more for Ni contact than Au.

For the sake of completeness, we intend to study whether the nature of metal contacts remains same with increasing thickness of MoS_2. Therefore, in Supplemental Material S1 [39], we discuss the DFT results of a bilayer metal/bilayer MoS_2 system and observe that the abovementioned metal/MoS_2 interfacial effects remain qualitatively similar.

C. Experimental results—Optical characterization of charge transfer

To support the analysis of metal induced charge transfer effects on the electronic properties of monolayer MoS_2, we now experimentally characterize a monolayer thick MoS_2 film in close proximity of metal. However, in a typical "MoS_2-bottom/metal-top" contact structure, it is difficult to characterize the inaccessible MoS_2 film underneath the metal. To avoid this problem, we prepare two sets (Au and Ni) of "metal-bottom/MoS_2-top" structures, as mentioned below. In this structure, we characterize the MoS_2 film both optically, as well as using Kelvin probe force microscopy (KPFM), while maintaining the proximity of metal states.

To obtain the proposed structure, Au lines of width 4 μm and separation 4 μm are obtained on a 285 nm thick SiO_2 layer on Si substrate using photolithography, followed by e-beam evaporation of metal and subsequent lift-off. A similar sample is prepared for Ni as well. Monolayers of MoS_2 layers are exfoliated on top of this, and only those monolayers are selected that connect at least two parallel metal lines. The thickness of the MoS_2 flake is confirmed by optical contrast in a microscope on the SiO_2 portion and also by measuring the separation between the A_{1g} and the E^1_{2g} Raman peaks.

Photoluminescence (PL) and Raman spectra were taken using a 532-nm laser focused using 100× objective lens. The Raman shift of the A_{1g} peak for monolayer MoS_2 on metals [Figs. 4(a) and 4(b)] shows a larger broadening compared with a sample on SiO_2, while the E^1_{2g} peak broadening remains almost substrate independent. Such broadening can be attributed to anharmonicity due to laser induced heating [40] and substrate induced doping [41]. However, larger broadening for monolayer samples on metals cannot attributed to the heating effect owing to better heat conduction by metal compared with SiO_2. This suggests that the additional broadening occurs due to metal induced charge transfer effect. By comparing the obtained Raman peak shift and full width at half maximum (FWHM) with the data presented in Ref. [41], we estimate the doping density in our monolayer MoS_2 samples to be $\approx 2.5 \times 10^{12}$ cm^{-2} and $\approx 9.7 \times 10^{11}$ cm^{-2} for Ni and Au substrates, respectively. Also, the PL intensity of

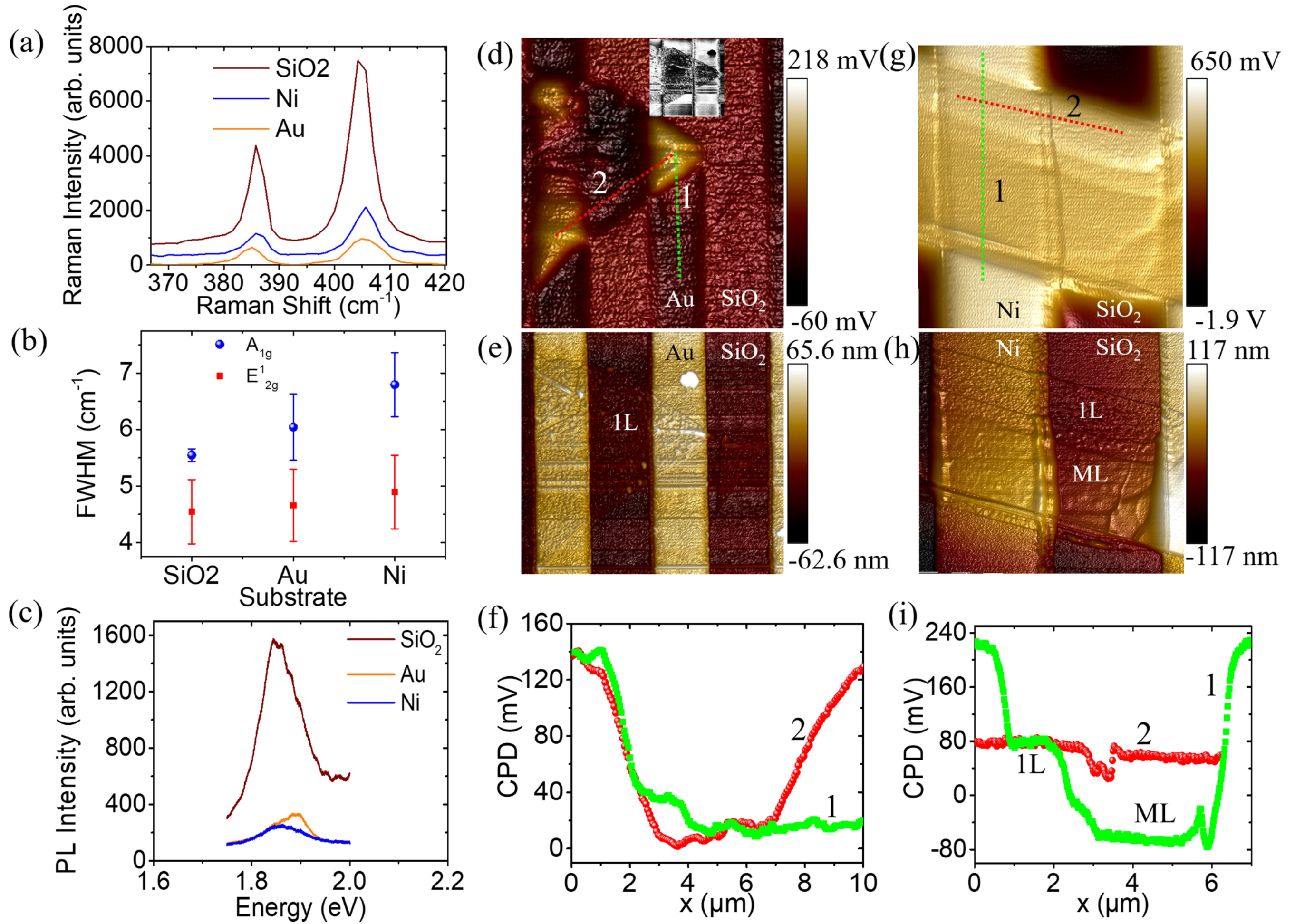

FIG. 4. Characterization of monolayer (1L) MoS_2 on metal and on SiO_2. (a) Raman intensity of 1L MoS_2 on various substrates. (b) The FWHM of Raman peaks as a function of substrate. (c) The PL spectra of 1L MoS_2 as a function of substrate, showing strong suppression on metal. (d) The CPD image of 1L MoS_2 on Au and SiO_2 lines showing strong work function differences. Inset. A 2D AFM image of the flake. (e) Corresponding AFM image of Au lines and triangular 1L flake. (f) Values of CPD along scan line 1 (MoS_2/Au-Au) and scan line 2 (MoS_2/Au-MoS_2/SiO_2-MoS_2/Au). (g) The CPD image of 1L/multilayer (ML) MoS_2 on Ni and SiO_2 lines. (h) Corresponding AFM image of Ni lines and MoS_2 flake. (i) Values of CPD along scan line 1 (Ni-1L MoS_2/Ni-ML MoS_2/Ni-Ni) and scan line 2 (1L MoS_2/Ni-1L MoS_2/SiO_2).

A_{1s} exciton peak is found to be dramatically suppressed for monolayers on metals [Fig. 4(c)], supporting interlayer charge transfer between metal and MoS_2.

We perform x-ray photoelectron spectroscopy (XPS) analysis of MoS_2 on SiO_2 and metal substrates, and the estimated Fermi level shift agrees qualitatively with the DFT predicted shifts (Supplemental Material S2 [39]). The XPS data indicates that the binding energies of the different core levels of MoS_2 on the metal substrates are blue shifted compared to the SiO_2 substrate samples. This is an indication of a relative shift of the Fermi level closer to the conduction band edge for the samples on Au and Ni substrates, suggesting *n*-type doping.

D. Effect of charge transfer—Creation of cascaded potential barriers

Because of the metal induced charge transfer, as depicted in Fig. 1, we introduce a model for electron injection from the source through three cascaded processes: (i) overcoming a vertical thermionic barrier height ϕ_V coupled with a tunneling barrier width d due to the van der Waals (vdW) gap between the top metal contact and the *modified* MoS_2 underneath the contact [diode D_V, shown in Fig. 5(a)]; (ii) horizontal transport through MoS_2 underneath the contact resulting in a current crowding resistance R_d [Fig. 5(b)]; and finally (iii) overcoming a horizontal barrier ϕ_H [diode D_H, shown in Fig. 5(c)] between *modified* MoS_2 under the contact and the undoped MoS_2 in the channel. Based on our *ab initio* calculation, two different scenarios may occur in determining ϕ_H: a metal contact, like Au, introduces limited gap states into the monolayer under the contact, and ϕ_H originates primarily due to the doping difference (between MoS_2 under contact and MoS_2 channel) induced built-in potential [left panel of Fig. 5(c)]. On the other hand, a metal contact, like Ni, induces a large density of gap states, which, in turn, results in strong Fermi level pinning at the MoS_2 under contact and channel MoS_2 junction, and hence a Schottky barrier [right panel of Fig. 5(c)].

Note that apart from charge transfer induced doping, the vertical barrier ϕ_V is also modulated due to the image force experienced by a carrier at the MoS_2 layer underneath the

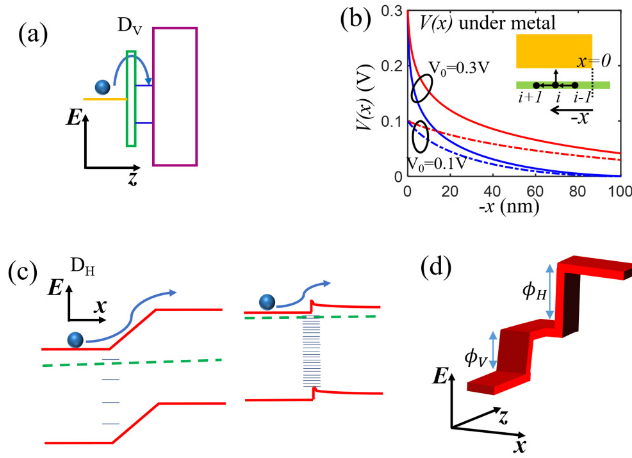

FIG. 5. Individual processes in cascade during carrier injection at the source junction. (a) The origin of the vertical diode D_V (with barrier ϕ_V) between the metal and the monolayer underneath the contact, through a tunneling vdW gap. (b) The variation of potential in the monolayer underneath the contact (current crowding regime) with $V_0 = V(x = 0)$. Red curves correspond to ten times better conductivity in the 2D film, compared with the blue curves. Inset: schematic of the calculation method in the current crowding regime. (c) Two possible origins of potential barrier ϕ_H in horizontal diode D_H at contact edge. Left panel: doping difference induced built-in barrier (weak interaction with contact). Right panel: Fermi level pinning induced Schottky barrier (strong interaction with contact). (d) A schematic 3D diagram depicting the different barriers encountered by the electron injected from the metal at the source end: the two barriers (ϕ_V and ϕ_H) with a sandwiched current crowding region in between.

contact [42,43], owing to the close proximity of conducting metal layer. For our top contact structure, as shown in Supplemental Material S3 [39], we estimate a barrier height lowering ($\Delta\phi_V$) of 0.25 eV due to image force.

To understand the nature of the different potential barriers, the KPFM images and the corresponding atomic force microscopy (AFM) images of the samples are shown in Figs. 4(d) and 4(e) for Au [and Figs. 4(g) and 4(h) for Ni]. All the metal lines were grounded during KPFM measurement. The KPFM results indicate the contact potential difference (CPD) between the tip and the sample, which allows us to infer the local work function differences $\Delta W = W_{\mathrm{tip}} - W_{\mathrm{sample}}$, where $W_{\mathrm{tip}} = 5.3\,\mathrm{eV}$. Using scan line 1 [Figs. 4(d)–4(f)], we note that $W_{\mathrm{tip}} - W_{\mathrm{Au}} \approx 0$; hence, $W_{\mathrm{Au}} = 5.3\,\mathrm{eV}$. We also see that $W_{\mathrm{Au}} - W_{\mathrm{MoS_2/Au}} = 0.12\,\mathrm{eV}$, inferring $W_{\mathrm{MoS_2/Au}} = 5.18\,\mathrm{eV}$. Using scan line 2, we obtain $W_{\mathrm{MoS_2/SiO_2}} - W_{\mathrm{MoS_2/Au}} = 0.13\,\mathrm{eV}$, which directly implies that the SBH between the two regions (ϕ_H) is 0.13 eV. For the Ni sample [Figs. 4(g)–4(i)], we have similarly obtained $W_{\mathrm{Ni}} = 5.06\,\mathrm{eV}$, $W_{\mathrm{MoS_2/Ni}} = 5.18\,\mathrm{eV}$, and $\phi_H = 20\,\mathrm{meV}$. As Raman data suggest that Ni causes higher doping than Au, a lower ϕ_H for Ni suggests a formation of Schottky barrier in D_H due to large density of band gap states in MoS_2 under Ni. Heavier source doping caused by Ni would have, otherwise, resulted in a larger ϕ_H in a purely doping difference induced barrier.

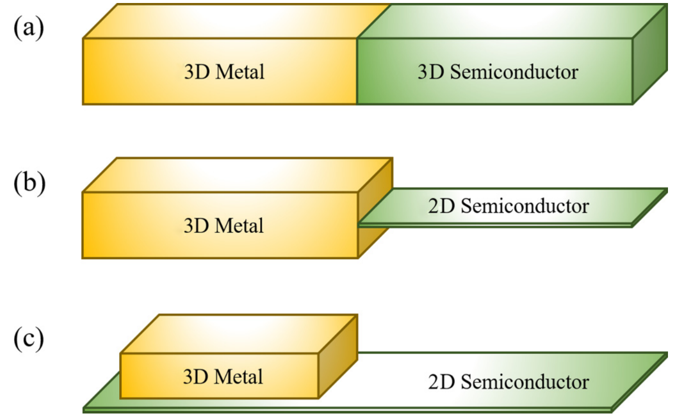

FIG. 6. Dimensionality of different metal/semiconductor contact topologies. (a) The 3D metal contacted with 3D semiconductor. (b) Edge contact between 3D metal and 2D semiconductor. (c) Top contact between 3D metal and 2D semiconductor.

IV. CARRIER INJECTION MODEL AT THE SOURCE FOR 2D/METAL CONTACT—A MODIFIED RICHARDSON EQUATION

A. Need for a modification in Richardson equation

The Richardson equation is often used for characterization of metal-semiconductor Schottky barriers and extraction of the corresponding barrier height [42]. However, the form of the Richardson equation to be used must conform to the dimensionality of the contact structure, as explained in Fig. 6. For example, when a three-dimensional (3D) metal is contacted with a bulk 3D semiconductor [Fig. 6(a)], the degree of the polynomial factor in T is 2 [42], which reduces to 1.5 when a 2D semiconductor is edge contacted with a 3D metal [44], as shown in Fig. 6(b). However, in our present case of a top contacted 2D semiconductor by a 3D metal [Fig. 6(c)], the carrier injection occurs through three cascaded processes, as mentioned before. A corresponding Richardson equation for such a structure is missing. Hence, we derive below a carrier transport model for each of the three processes and then combine them in cascade to obtain an effective Richardson equation.

B. Vertical contact diode

To obtain the effective Richardson equation that describes the vertical charge injection mechanism, we take the MoS_2 portion underneath the metal contact as a doped ultrathin semiconductor. We model D_V [Fig. 5(a)] as two different planes of carriers are separated by a vdW gap d. In the Appendix, we derive a modified Richardson equation for the vertical diode D_V by following the approach of Bardeen [45] and Tersoff [46]

$$J_v = A'_V e^{-2k_0 d} T^{\alpha_V} e^{-q\phi_V/k_B T} = A^*_V T^{\alpha_V} e^{-q\phi_V/k_B T} \quad (1)$$

with $\alpha_V = 1$ and $\phi_V = \phi_{V0} - \eta V_g - \gamma V_{ds}$. ϕ_{V0} as the barrier height without any bias, V_g is the backgate voltage, V_{ds} is the applied drain bias grounding the source, and η and γ are screening dependent parameters (see Appendix).

$A_V^* = A_V' e^{-2k_0 d}$ is the modified Richardson constant and k_0 is a constant defined in the Appendix.

C. Current crowding regime

We understand the origin of current crowding effect and a corresponding resistance R_d as follows: As shown in the inset of Fig. 5(b), due of continuity of current flow, at any point, the loss due to the vertical current must be compensated by reduction in the horizontal current. Thus, at ith node, we obtain the voltage $V(x)$ from the continuity equation: $\sigma[\frac{V_{i-1}-V_i}{\Delta x} - \frac{V_i - V_{i+1}}{\Delta x}] = J_v(x)\Delta x$ where σ is the in-plane conductivity of the 2D material under the metal. This reduces to $\frac{d^2V(x)}{dx^2} = \frac{\zeta}{\sigma} e^{qV(x)/k_BT}$ with $\zeta = A_V^* T^{\alpha_V} e^{-q(\phi_{V0} - \eta V_g)/k_BT}$. $V(x)$ can be solved analytically to obtain

$$V(x) = -\frac{2}{\beta} \ln\left[\cos\left\{\frac{\beta}{2}(D_0 + \lambda x)\right\}\right] \tag{2}$$

where $\beta = \frac{q}{k_BT}, \lambda = (\frac{2\zeta}{\beta\sigma})^{1/2}$, and $D_0 = -\frac{2}{\beta}\tan^{-1}(\sqrt{e^{\beta V_0} - 1})$. Here, q is the magnitude of electron charge, k_B is the Boltzmann constant, T is the temperature, and $V_0 = V(x = 0)$. $V(x)$ underneath the contact is plotted in Fig. 5(b) showing the extent of current transfer.

D. Horizontal diode

We model D_H [Fig. 5(c)] as a 2D diode in the plane of the monolayer MoS_2 with a barrier height ϕ_H. The corresponding Richardson equation is obtained by using the approach described in Ref. [44]

$$J_H = A_H^* T^{\alpha_H} e^{-q\phi_H/k_BT} \tag{3}$$

with $\alpha_H = 1.5$.

E. Combined effect—Effective Richardson equation

Note that both α_V and α_H differ from the conventional value of $\alpha = 2$ for three dimensions [42]. The combined processes are schematically depicted in Fig. 5(d). The injected electrons experience an effective barrier due to cascading effect of D_V, R_d, and D_H, following an effective Richardson equation

$$J = A_{\text{eff}}^* T^{\alpha_{\text{eff}}} e^{-q\phi_{B,\text{eff}}/k_BT} \tag{4}$$

where the effective barrier height $\phi_{B,\text{eff}} \leqslant \phi_V + \phi_H$. The equality holds only when either of ϕ_V and ϕ_H is negligible (that is, zero reflection from one of the diodes) and the transport underneath the metal is near ballistic. Also, since ϕ_V and ϕ_H vary with biasing conditions, α_{eff} varies in the range $1 \leqslant \alpha_{\text{eff}} \leqslant 1.5$.

V. A TLM BASED METHODOLOGY FOR EFFECTIVE BARRIER HEIGHT EXTRACTION

A. Existing issues in barrier height extraction

In TMDC literature, both $\alpha_{\text{eff}} = 2$ [16,17] or $\alpha_{\text{eff}} = 1.5$ [15,47] have been used for barrier height extraction. Apart from the choice of α_{eff}, the extracted SBH is usually confounded due to another reason: the channel resistance does not remain constant with temperature owing to strong dependence of carrier mobility on temperature in these thin layers [29]. Hence, the Richardson equation does not completely describe the temperature dependence of the total current. The extracted barrier height is usually underestimated as mobility degrades with temperature.

B. Proposed methodology

To nullify the temperature dependent channel resistance effect, we employ TLM structure by fabricating a set of backgated and top metal contacted devices with varying channel length. Monolayer MoS_2 flakes are first exfoliated on a Si wafer covered by 285 nm SiO_2, which acts as the backgate dielectric. To have uniform rectangular channel, the monolayer flakes are first patterned by electron beam lithography followed by reactive ion etching (RIE) for 20 s in BCl_3 (15 sccm) and Ar (60 sccm), with an RF power of 50 W and chamber pressure of 4.5 mTorr, at $-10°$ C. The second level of electron beam lithography is used to define top metal contacts. Respective metals [namely, (i) 50 nm Au or (ii) 7 nm Ni/50 nm Au) are deposited using electron beam evaporation at a 4.5×10^{-7} Torr, followed by metal lift-off in acetone. For the backgate, aluminium is evaporated on the back side after a dilute hydrofluoric acid (HF) treatment.

A set of devices with Raman mapping and scanning electron micrograph are shown in Fig. 7(a). The I_{ds}-V_g characteristics of a typical device with Au and Ni contacts are shown in Fig. 7(b) at different temperatures (215 K to 290 K). The electrical measurements of the devices were done at a vacuum level of 2.25×10^{-6} Torr using an Agilent B1500 device analyzer. All of our Ni contacted devices exhibit a lower threshold voltage compared with the Au contacted devices. This suggests strong Fermi level pinning close to the conduction band edge at the junction between the MoS_2 underneath the contact region and the MoS_2 in the channel region. This, in turn, electrically dopes the channel n-type [12]. Figure 7(c) shows almost hysteresis-free drivability of 52 μA/μm in a 300-nm channel length Au/monolayer device at $V_g = 80$ V and $V_{ds} = 2$ V.

Figure 8(a) shows the method of extraction of the contact resistance, where the total contact resistance (R_{cT}) is obtained from a linear fit of total resistance: $R_TW = R_{sh}L + R_{cT}W$ and subsequent extrapolation of the line at $L = 0$. Here, R_{sh} and W are the sheet resistance of the channel and width of the devices, respectively. The extracted R_{cT} is a strong function of device operating condition (V_g, V_{ds}). Note that $R_{cT} = R_{cS} + R_{cD}$ is the total contact resistance offered by the source and drain sides, which are generally unequal. This is due to the presence of finite thermal barrier in the source side, while the electrons do not experience any such barrier on the drain side. However, at large V_g and V_{ds}, the source side barrier is diminished, and both sides contribute almost equally to R_{cT}. Owing to lack of a thermal barrier, the drain side is also expected to be weakly dependent on V_g and V_{ds}, leading to an approximate estimation of the drain side contact resistance as $R_{cD} \approx 0.5\times R_{cT}(V_{g,\max}, V_{ds,\max})$ which is bias independent. The source side component of R_{cT} is, thus, extracted as $R_{cS}(V_g, V_{ds}) = R_{cT}(V_g, V_{ds}) - R_{cD} \approx R_{cT}(V_g, V_{ds}) - 0.5\times R_{cT}(V_{g,\max}, V_{ds,\max})$. Thus, a current $I_c = \frac{V_{ds}}{R_{cS}}$ will be delivered by the source contact diode if the complete bias V_{ds} is hypothetically applied across only the

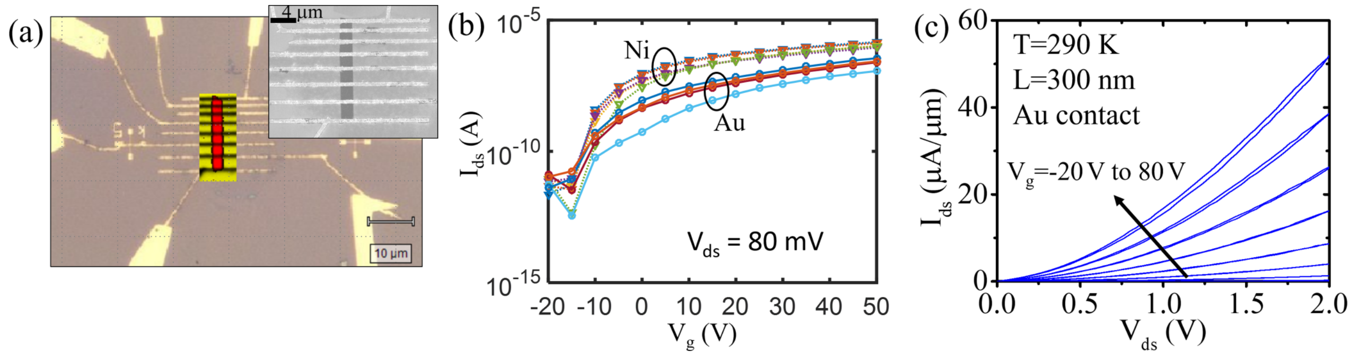

FIG. 7. Electrical extraction of effective barrier height. (a) Optical image and the corresponding Raman mapping of a typical TLM device. In the Raman map, red patch corresponds to the monolayer MoS_2 and the green signal is from Si. Inset. A scanning electron microscopy image of the device. (b) I_{ds}-V_g plot of Au and Ni contacted device at multiple temperatures. Ni devices show lower threshold voltage. (c) Forward and reverse I_{ds}-V_{ds} sweep of a backgated monolayer transistor with a 300-nm channel length, showing 52 μA/μm drive current at $V_{ds} = 2$ V and $V_g = 80$ V.

source contact diode. This is schematically explained in Fig. 8(b). I_c characterizes the source contact diode without any confounding effect from the channel resistance or the drain. Using $\alpha_{\text{eff}} = 1$, Fig. 8(c) shows good linear fit between $\ln(I_c T^{-\alpha_{\text{eff}}})$ with $\frac{q}{k_B T}$, allowing us to unambiguously extract $\phi_{B,\text{eff}}$. The extracted $\phi_{B,\text{eff}}$ for Au is plotted as a function of V_g and V_{ds} in Figs. 9(a) and 9(b). In Supplemental Material S4 [39], the extraction is performed with $\alpha_{\text{eff}} = 1.5$ showing a difference of $\sim$10 meV in the extracted barrier height. The Ni contacted devices [Figs. 9(c) and 9(d)] consistently show lower $\phi_{B,\text{eff}}$ compared with Au, in agreement with the KPFM analysis discussed before.

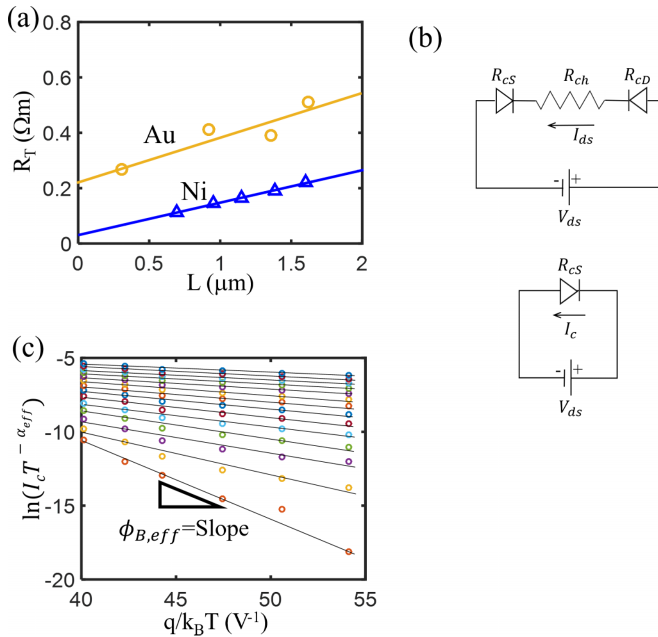

FIG. 8. Barrier height extraction methodology. (a) A typical TLM fit for Au and Ni devices with intercept at $L = 0$ corresponding to R_{cT}. (b) Method of calculation of $I_c = V_{ds}/R_{cS}$, which is the hypothetical current obtained when V_{ds} is applied across the source contact diode. (c) I_c is used in a Richardson plot at different biasing conditions. The slopes of the linear fits correspond to the effective barrier height.

C. Validation with simulation

For insight into the V_g dependence of $\phi_{B,\text{eff}}$, we solve 1D CPS equations along the vertical direction of the device, both at the channel regime and at the contact regime (see Supplemental Material S5 [39]). From the simulated potential, the barrier height is extracted in Fig. 10, which will be valid for small V_{ds} due to the 1D nature of the equations. Using only channel doping as a fitting parameter, we can obtain good agreement between the simulation (red lines) and the TLM extracted SBH. The deviation of $\phi_{B,\text{eff}}(V_g)$ from linearity at higher gate voltage arises due to strong gate field screening. Using KPFM extracted ϕ_H in Fig. 4 and assuming $\phi_{B,\text{eff}} \approx \phi_V + \phi_H$, the individual components ϕ_V and ϕ_H are extracted at $V_g = 0$. Also, using this $\phi_V(V_g = 0)$, we extract the doping of the monolayer MoS_2 film underneath the contact, and using the same, the ϕ_V at nonzero V_g is also simulated (blue lines). At the

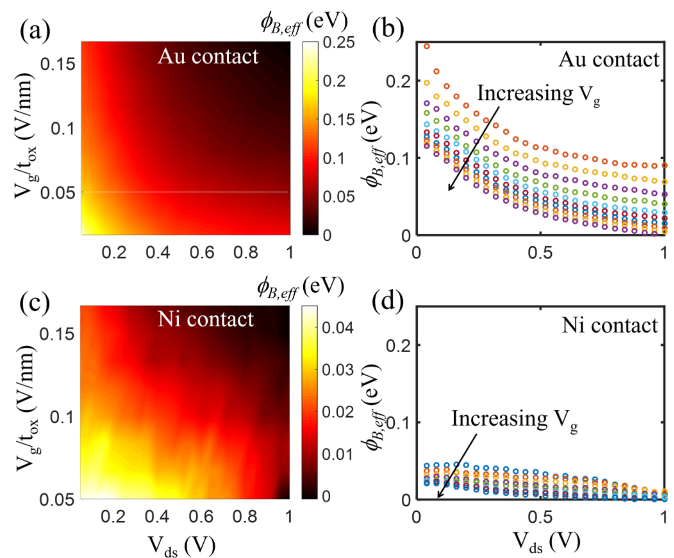

FIG. 9. Device operating condition dependent extracted barrier height. (a) The effective barrier height for Au-MoS_2 contact, as extracted from TLM, is plotted as a function of V_{ds} and gate electric field. (b) Horizontal slices of (a) at different gate electric field. (c) and (d) The effective barrier height for Ni-MoS_2 contact.

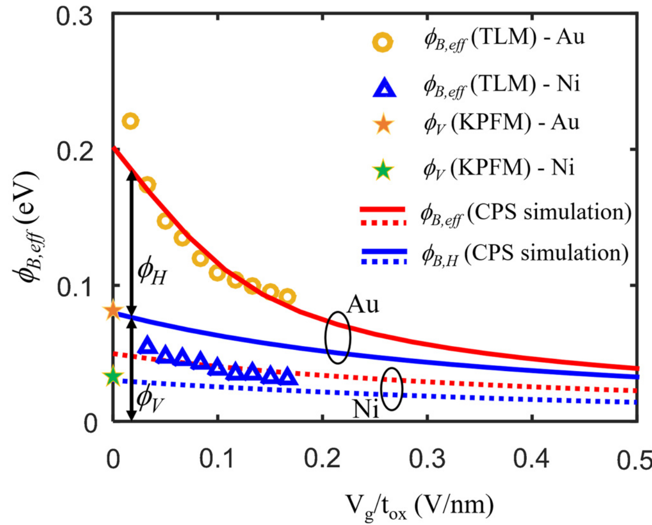

FIG. 10. Experimental validation of thermionic model. Comparison of coupled Poisson Schrödinger (CPS) solution predicted $\phi_{B,\mathrm{eff}}$ (shown in red solid line for Au and red broken lines for Ni) and the corresponding TLM extracted value (golden circle for Au and blue triangle for Ni), at small V_{ds} using channel doping ($6.3\times10^{9}\ \mathrm{cm}^{-2}$ for Au and $2.24\times10^{12}\ \mathrm{cm}^{-2}$ for Ni) as fitting parameter. The star symbols indicate ϕ_V at $V_{\mathrm{g}} = 0$, which is obtained by subtracting the KPFM extracted ϕ_H from simulated $\phi_{B,\mathrm{eff}}$. The blue lines (solid for Au and broken for Ni) correspond to ϕ_V at nonzero V_{g} and are obtained by fitting a doping concentration ($7.0\times10^{11}\ \mathrm{cm}^{-2}$ for Au and $4.76\times10^{12}\ \mathrm{cm}^{-2}$ for Ni) underneath the contact corresponding to the star.

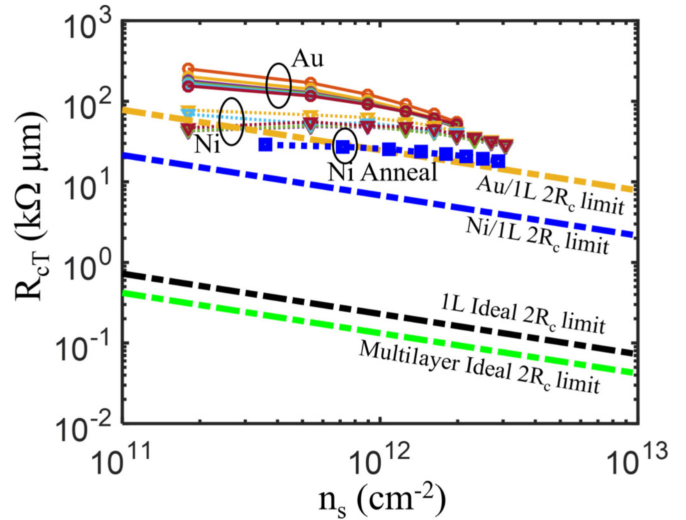

FIG. 11. Limits of contact resistance. The extracted total contact resistance $R_{\mathrm{cT}} = R_{\mathrm{cS}} + R_{\mathrm{cD}}$ for Au and Ni at different temperatures (215 to 290 K) are shown as a function of the 2D sheet carrier density. Annealed Ni contact is also shown at 290 K. The corresponding lower limits achievable for Au ($d = 3$ Å, $W_{\mathrm{m}} = 5.3$ eV), Ni ($d = 2.2$ Å, $W_{\mathrm{m}} = 5.06$ eV), and an ideal contact ($d = 0$) are shown for comparison. For monolayer (1L) and multilayer (ML), $g_{\mathrm{v}} = 2$ and $g_{\mathrm{v}} = 6$ are used, respectively. Tunneling vdW gap (d) values are obtained from DFT calculation, and metal work function (W_{m}) are obtained from KPFM results.

larger gate field, ϕ_H almost collapses, and ϕ_V dominates the total barrier. With an increase in V_{ds}, ϕ_V also is suppressed, and the device enters a "*zero thermal barrier*" regime of operation [bottom right corner of Figs. 9(b) and 9(d)], where only d and R_{d} control the contact resistance.

VI. CONTACT RESISTANCE AND ITS LANDAUER LIMIT FOR 2D TMDC/METAL CONTACT INTERFACE

In Fig. 11, R_{cT} of the Au and Ni devices is plotted as a function of the 2D sheet carrier density (n_{s}) at different temperatures. n_{s} is obtained as $n_{\mathrm{s}} = C_{ox}(V_{\mathrm{g}} - V_{\mathrm{t}})/q$. At T = 290 K, the gate field = 0.167 V/nm and $V_{\mathrm{ds}} = 1$ V, the contact resistance ($R_{\mathrm{c}} = R_{\mathrm{cT}}/2$) between monolayer $\mathrm{MoS_2}$ and Ni (Au) has been found to be 14 kΩ μm (23 kΩ μm). This reduces to 9 kΩ μm (for Ni) after vacuum anneal at 127 °C for 1 h. The extracted values of R_{cT} from another set of Au and Ni TLMs are shown in Supplemental Material S6 [39].

To investigate how these values compare with the fundamental limit of contact resistance achievable in these structures, we use the Landauer approach [48] to find the conductance in a monolayer $\mathrm{MoS_2}$/metal contact: $G = (\frac{2q^2}{h})g_v M T_{\mathrm{eff}}$, where h is Plank's constant, g_{v} is valley degeneracy (=2 for monolayer $\mathrm{MoS_2}$ arising from degenerate K and K' valleys), and M is number of current carrying modes per valley. T_{eff} is the effective transmission probability through the three cascaded processes described earlier and is given by $T_{\mathrm{eff}} = \frac{1}{\frac{1}{T_V}+\frac{1}{T_d}+\frac{1}{T_H}-2}$. For maximum transmission limit, $T_{\mathrm{eff,max}} = e^{-2k_0 d}$ is obtained at the zero thermal barrier and ballistic limit, by noting that $T_{V,\mathrm{max}} = e^{-2k_0 d}$ (tunneling through zero thermal barrier vdW gap in $\mathrm{D_V}$), $T_{d,\mathrm{max}} = 1$ (ballistic limit of $\mathrm{MoS_2}$ underneath metal), and $T_{H,\mathrm{max}} = 1$ (zero thermal barrier in $\mathrm{D_H}$). At the low temperature limit, only electrons at Fermi level take part in conduction, and hence $k_0 = \frac{(2m^*\varphi_{\mathrm{avg}})^{1/2}}{\hbar}$ (See the Appendix). Here, we assumed $\varphi_{\mathrm{avg}} = 0.5(W_m + \chi_{\mathrm{MoS_2}})$. The number of modes of a 2D conducting channel is given by [48]: $M = \mathrm{Int}[\sqrt{\frac{2m^* W^2 \Delta E}{\pi^2\hbar^2}}] \approx W\sqrt{\frac{2n_{\mathrm{s}}}{g_{\mathrm{v}}\pi}}$, where n_{s} is given by $n_{\mathrm{s}} = g_{\mathrm{v}}\frac{m^*}{\pi\hbar^2}\Delta E$, ignoring Fermi-Dirac broadening. Here Int[.] is the maximum integer function. Hence,

$$R_{\mathrm{c,min}} W = \frac{W}{G_{\mathrm{max}}} = \left(\frac{h}{2q^2}\right) e^{2k_0 d}\sqrt{\frac{\pi}{2g_{\mathrm{v}} n_{\mathrm{s}}}}. \tag{5}$$

In Fig. 6(b), the $2R_{\mathrm{c,min}}W$ limits are plotted for Au, Ni, and also for an ideal contact, where $d = 0$ is assumed. For comparison, the ideal multilayer limit is also shown using $g_{\mathrm{v}} = 6$. The obtained limits clearly allow provision for further technological improvement. Note that at smaller V_{g}, the extracted R_{c} decreases with an increase in temperature, due to enhanced thermionic emission efficiency. However, the trend diminishes and eventually reverses at higher bias (see Supplemental Material S7 [39]), where the thermionic emission efficiency does not change appreciably due to negligible barrier, but the carrier scattering under contact increases with an increase in temperature, in turn, increasing contact resistance.

VII. CONCLUSION

In conclusion, using a combination of theoretical and experimental techniques, we investigated the nature of the carrier injection at the junction between a monolayer MoS_2 and the contacting metal. We have shown that the charge transfer between contact metal and MoS_2 underneath plays a key role in such a contact, where the carrier from source is injected via two cascaded thermal barriers. The corresponding Richardson equation of such a Schottky diode requires appropriate modification in the power of temperature. At large gate and drain bias, both Au and Ni offer zero effective thermal barrier contact, where the contact resistance is limited by the tunneling vdW gap and the conductivity of the monolayer underneath the contact. At this zero-barrier condition, the fundamental lower limits of contact resistance are obtained theoretically using the Landauer approach. The insights obtained will be useful in designing well-behaved contacts for high performance 2D electronic and optoelectronic devices.

ACKNOWLEDGMENTS

D.K. acknowledges support from BARC-ANUPAM supercomputing facility and help from T. K. Maji. K.M. acknowledges the support of a start-up grant from Indian Institute of Science (IISc), Bangalore, the support of a grant under Space Technology Cell, Indian Space Research Organization (ISRO)-IISc, and the support of grants under Ramanujan Fellowship, Early Career Award, and Nano Mission from the Department of Science and Technology (DST), Government of India.

D.S. and S.K. contributed equally to this work.

APPENDIX: DERIVATION OF RICHARDSON EQUATION FOR VERTICAL CURRENT INJECTION IN METAL/2D SEMICONDUCTOR VERTICAL JUNCTION (DIODE D_V)

The current injection mechanism in the vertical diode is a combined process of thermionic emission and tunneling through the vdW gap (d) between the metal surface and the 2D material. To model this carrier injection, we assume the 2D material as an almost perfect 2D plane. Assuming effective mass approximation (free electrons in the plane of the metal surface and the 2D material), we write the wave function of the electron at the metal surface as

$$\psi_m = {\Omega_m}^{-1/2} e^{-k_m(d-z)} e^{i\overline{k_\parallel^m}.\bar{\rho}} \tag{A1}$$

and at the 2D semiconductor as

$$\psi_s = {\Omega_s}^{-1/2} e^{-k_s z} e^{i\overline{k_\parallel^s}.\bar{\rho}} \tag{A2}$$

where $z = 0$ is assumed as the plane of the 2D semiconductor. Ω_m and Ω_s are, respectively, the metal and semiconductor area under consideration. Here, $\bar{\rho}$ is the position vector in the plane of the metal surface or the 2D material, and $\overline{k_\parallel^m}$ ($\overline{k_\parallel^s}$) is the corresponding in-plane wave vector in the metal (semiconductor) plane. k_m and k_s are the decay constant of the wave functions in the vdW gap between the metal and 2D material and given by $k_m = \frac{[2m^*(W_m-\epsilon)]^{1/2}}{\hbar}$ and $k_s = \frac{[2m^*(\chi_s-\epsilon)]^{1/2}}{\hbar}$ at energy ϵ. Here, m^* is the carrier effective mass, W_m represents the work function of the metal, and χ_s is the electron affinity of the 2D semiconductor. The major contribution of the current comes from energy states close to the band edge of the 2D material; hence, W_m, $\chi_s \gg \epsilon$, allowing us to treat k_m, k_s as independent of energy. Assuming elastic tunneling and under small bias V, the tunneling current can be obtained using first order perturbation theory:

$$I = \frac{2\pi q}{\hbar} \sum_{ms} |C_{ms}|^2 f(E_m + qV)\{1 - f(E_s)\}\delta(E_m - E_s) \tag{A3}$$

Here, q is the magnitude of electron charge, $\hbar = h/2\pi$ with h is Planck constant, $E_{m(s)}$ is the energy of corresponding state in the metal (2D semiconductor), and $f(E)$ is the Fermi-Dirac probability of carrier occupation at energy E. The tunneling matrix element has been shown to be [46]

$$C_{ms} = -\frac{\hbar^2}{2m^*} \int d\bar{A}.(\psi_m^* \bar{\nabla}\psi_s - \psi_s \bar{\nabla}\psi_m^*) \tag{A4}$$

Using the wave functions in Eqs. (A1) and (A2), one can evaluate the matrix element in Eq. (A4) to

$$C_{ms} = -\frac{\pi\hbar^2}{m^*\Omega}(k_m + k_s) e^{-k_m d} e^{(k_m - k_s)z}\, \delta(\overline{k_\parallel^m} - \overline{k_\parallel^s}) \tag{A5}$$

where $\Omega = (\Omega_m \times \Omega_s)^{1/2}$. Using Eqs. (A3) and (A5) and noting that only those electrons with an energy more than $q\phi_V$ can tunnel through the vdW gap, we can rewrite the current density as

$$J_v = \kappa \frac{2\pi^3 q\hbar^3}{m^{*2}} (k_m + k_s)^2 e^{-2k_m d} e^{2(k_m - k_s)z} \sum_{\substack{\overline{k_\parallel^m}, \overline{k_\parallel^s} \\ E_m > q\phi_V}} [f(E_m + qV)\{1 - f(E_s)\}\delta(E_m - E_s)\delta(\overline{k_\parallel^m} - \overline{k_\parallel^s})] \tag{A6}$$

where κ is a normalization constant. The delta functions under the summation ensure conservation of in-plane momentum, as well as conservation of energy during the elastic tunneling process. Note that due to continuity equation, the current must be independent of z, which ensures that $k_m = k_s (=k_0)$. This is expected, as we are only considering elastic tunneling.

For further evaluation, we convert the summation over 2D k space into integral over energy, as follows:

$$J_v = \kappa \frac{8\pi^3 q\hbar^3}{m^{*2}} {k_0}^2 e^{-2k_0 d} \int_{q(\phi_{V0} - \eta V_g)}^{\infty} dE\ D(E) e^{-(E + q\gamma V_{ds})/k_B T} \tag{A7}$$

Here, we approximated the Fermi-Dirac distribution as Boltzmann distribution and also assumed $1 - f(E_s) \approx 1$. k_B is the Boltzmann constant and T is the temperature. The DOS is given by $D(E) = \mathrm{Min}\{D_m(E), D_s(E)\} = D_s(E) = g_v \frac{m^*}{\pi\hbar^2}$, where g_v is the valley degeneracy and is 2 for monolayer MoS_2 arising from K and K' valleys. In Eq. (A7), $V = \gamma V_{ds}$ is the difference between the quasi-Fermi levels of the metal and the portion of the 2D material under the metal and depends on the applied bias V_{ds}. Similarly, application of a positive back gate voltage V_g pushes down the conduction band edge of the 2D material underneath the metal and hence suppresses the effective barrier height by ηV_g. For small V_g, η is a constant and depends on how well the gate is electrostatically coupled to the 2D material under the metal contact. However, at larger V_g, η reduces significantly owing to strong screening [49]. ϕ_{V0} is the barrier height in the absence of any external bias. Also, assuming only states close to the Fermi level contribute to the current, we take $k_0{}^2 \approx \frac{2m^*\varphi_{avg}}{\hbar^2}$, where $\varphi_{avg} = 0.5(W_m + \chi_{MoS_2})$. Substituting in Eq. (A7), the expression for current density is obtained as

$$J_v = A'_V e^{-2k_0 d} T e^{-q(\phi_{V0} - \eta V_g - \gamma V_{ds})/k_B T} = A^*_V T e^{-q\phi_V/k_B T} \tag{A8}$$

where $A'_V \propto \frac{16\pi^3 q}{\hbar m^*} g_v k_B \varphi_{avg}$, $A^*_V = A'_V e^{-2k_0 d}$, and $\phi_V = \phi_{V0} - \eta V_g - \gamma V_{ds}$. Equation (A8) represents the modified Richardson equation for out of plane electron injection from metal into the 2D semiconductor.

[1] K. F. Mak, C. Lee, J. Hone, J. Shan, and T. F. Heinz, Atomically Thin MoS_2: A New Direct-Gap Semiconductor, Phys. Rev. Lett. **105**, 136805 (2010).

[2] Q. H. Wang, K. Kalantar-Zadeh, A. Kis, J. N. Coleman, and M. S. Strano, Electronics and optoelectronics of two-dimensional transition metal dichalcogenides, Nat. Nanotechnol. **7**, 699 (2012).

[3] A. Pospischil, M. Furchi, and T. Mueller, Solar-energy conversion and light emission in an atomic monolayer *p-n* diode, Nat. Nanotechnol. **9**, 257 (2014).

[4] B. Baugher, H. Churchill, Y. Yang, and P. Jarillo-Herrero, Optoelectronic devices based on electrically tunable *p-n* diodes in a monolayer dichalcogenide, Nat. Nanotechnol. **9**, 262 (2014).

[5] O. Lopez-Sanchez, D. Lembke, M. Kayci, A. Radenovic, and A. Kis, Ultrasensitive photodetectors based on monolayer MoS_2, Nat. Nanotechnol. **8**, 497 (2013).

[6] W. J. Yu, Y. Liu, H. Zhou, A. Yin, Z. Li, Y. Huang, and X. Duan, Highly efficient gate-tunable photocurrent generation in vertical heterostructures of layered materials, Nat. Nanotechnol. **8**, 952 (2013).

[7] K. Majumdar, C. Hobbs, and P. D. Kirsch, Benchmarking transition metal dichalcogenide MOSFET in the ultimate physical scaling limit, IEEE Electron Device Lett. **35**, 402 (2014).

[8] B. Radisavljevic, A. Radenovic, J. Brivio, V. Giacometti, and A. Kis, Single-layer MoS_2 transistors, Nat. Nanotechnol. **6**, 147 (2011).

[9] A. Allain, J. Kang, K. Banerjee, and A. Kis, Electrical contacts to two-dimensional semiconductors, Nat. Mater. **14**, 1195 (2015).

[10] Y. Xu, C. Cheng, S. Du, J. Yang, B. Yu, J. Luo, W. Yin, E. Li, S. Dong, P. Ye, and X. Duan, Contacts between two- and three-dimensional materials: Ohmic, Schottky, and *p-n* heterojunctions, ACS Nano **10**, 4895 (2016).

[11] F. Léonard and A. A. Talin, Electrical contacts to one- and two-dimensional nanomaterials, Nat. Nanotechnol. **6**, 773 (2011).

[12] S. Kallatt, G. Umesh, N. Bhat, and K. Majumdar, Photoresponse of atomically thin MoS_2 layers and their planar heterojunctions, Nanoscale **8**, 15213 (2016).

[13] M. Buscema, M. Barkelid, V. Zwiller, H. S. J. van der Zant, G. A. Steele, and A. Castellanos-Gomez, Large and tunable photothermoelectric effect in single-layer MoS_2, Nano Lett. **13**, 358 (2013).

[14] S. Das, H.-Y. Y. Chen, A. V. Penumatcha, and J. Appenzeller, High performance multi-layer MoS_2 transistors with scandium contacts, Nano Lett. **13**, 100 (2012).

[15] J.-R. Chen, P. M. Odenthal, A. G. Swartz, G. C. Floyd, H. Wen, K. Y. Luo, and R. K. Kawakami, Control of Schottky barriers in single layer MoS_2 transistors with ferromagnetic contacts, Nano Lett. **13**, 3106 (2013).

[16] A. Dankert, L. Langouche, M. V. Kamalakar, and S. P. Dash, High-performance molybdenum disulfide field-effect transistors with spin tunnel contacts, ACS Nano **8**, 476 (2014).

[17] C. D. English, G. Shine, V. E. Dorgan, K. C. Saraswat, and E. Pop, Improved contacts to MoS_2 transistors by ultra-high vacuum metal deposition, Nano Lett. **16**, 3824 (2016).

[18] H. Fang, M. Tosun, G. Seol, T. C. Chang, K. Takei, J. Guo, and A. Javey, Degenerate *n*-doping of few-layer transition metal dichalcogenides by potassium, Nano Lett. **13**, 1991 (2013).

[19] W. S. Leong, X. Luo, Y. Li, K. H. Khoo, S. Y. Quek, and J. T. L. Thong, Low resistance metal contacts to MoS_2 devices with nickel-etched-graphene electrodes, ACS Nano **9**, 869 (2014).

[20] Y. Liu, H. Wu, H.-C. Cheng, S. Yang, E. Zhu, Q. He, M. Ding, D. Li, J. Guo, N. O. Weiss, Y. Huang, and X. Duan, Toward barrier free contact to molybdenum disulfide using graphene electrodes, Nano Lett. **15**, 3030 (2015).

[21] S. McDonnell, C. Smyth, C. L. Hinkle, and R. M. Wallace, MoS_2 -titanium contact interface reactions, ACS Appl. Mater. Interfaces **8**, 8289 (2016).

[22] L. Yang, K. Majumdar, H. Liu, Y. Du, H. Wu, M. Hatzistergos, P. Y. Hung, R. Tieckelmann, W. Tsai, C. Hobbs, and P. D. Ye, Chloride molecular doping technique on 2D materials: WS_2 and MoS_2, Nano Lett. **14**, 6275 (2014).

[23] H. Liu, A. T. Neal, and P. D. Ye, Channel length scaling of MoS_2 MOSFETs, ACS Nano **6**, 8563 (2012).

[24] X. Cui, G.-H. Lee, Y. D. Kim, G. Arefe, P. Y. Huang, C.-H. Lee, D. A. Chenet, X. Zhang, L. Wang, F. Ye, F. Pizzocchero, B. S. Jessen, K. Watanabe, T. Taniguchi, D. A. Muller, T. Low, P. Kim, and J. Hone, Multi-terminal transport measurements of MoS_2 using a van der Waals heterostructure device platform, Nat. Nanotechnol. **10**, 534 (2015).

[25] Y. Liu, J. Guo, Y.-C. Wu, E. Zhu, N. O. Weiss, Q. He, H. Wu, H.-C. Cheng, Y. Xu, I. Shakir, Y. Huang, and X. Duan, Pushing

the performance limit of sub-100 nm molybdenum disulfide transistors, Nano Lett. **16**, 6337 (2016).

[26] H. Fang, S. Chuang, T. C. Chang, K. Takei, T. Takahashi, and A. Javey, High-performance single layered WSe_2 *p*-FETs with chemically doped contacts, Nano Lett. **12**, 3788 (2012).

[27] H. Liu, M. Si, Y. Deng, A. T. Neal, Y. Du, S. Najmaei, P. M. Ajayan, J. Lou, and P. D. Ye, Switching mechanism in single-layer molybdenum disulfide transistors: An insight into current flow across Schottky barriers, ACS Nano **8**, 1031 (2014).

[28] R. Kappera, D. Voiry, S. E. Yalcin, B. Branch, G. Gupta, A. D. Mohite, and M. Chhowalla, Phase-engineered low-resistance contacts for ultrathin MoS_2 transistors, Nat. Mater. **13**, 1128 (2014).

[29] D. Jariwala, V. K. Sangwan, D. J. Late, J. E. Johns, V. P. Dravid, T. J. Marks, L. J. Lauhon, and M. C. Hersam, Band-like transport in high mobility unencapsulated single-layer MoS_2 transistors, Appl. Phys. Lett. **102**, 173107 (2013).

[30] J. Kang, W. Liu, and K. Banerjee, High-performance MoS_2 transistors with low-resistance molybdenum contacts, Appl. Phys. Lett. **104**, 093106 (2014).

[31] D. Jena, K. Banerjee, and G. Xing, Intimate contacts, Nat. Mater. **13**, 1076 (2014).

[32] F. Xia, V. Perebeinos, Y.-M. Lin, Y. Wu, and P. Avouris, The origins and limits of metal-graphene junction resistance, Nat. Nanotechnol. **6**, 179 (2011).

[33] W. Chen, E. J. G. Santos, W. Zhu, E. Kaxiras, and Z. Zhang, Tuning the electronic and chemical properties of monolayer MoS_2 adsorbed on transition metal substrates, Nano Lett. **13**, 509 (2013).

[34] J. Kang, W. Liu, D. Sarkar, D. Jena, and K. Banerjee, Computational Study of Metal Contacts to Monolayer Transition-Metal Dichalcogenide Semiconductors, Phys. Rev. X **4**, 031005 (2014).

[35] K. Dolui, A. Narayan, I. Rungger, and S. Sanvito, Efficient spin injection and giant magnetoresistance in Fe/ MoS_2 /Fe junctions, Phys. Rev. B **90**, 041401(R) (2014).

[36] T. Garandel, R. Arras, X. Marie, P. Renucci, and L. Calmels, Electronic structure of the Co(0001)/MoS_2 interface and its possible use for electrical spin injection in a single MoS_2 layer, Phys. Rev. B **95**, 075402 (2017).

[37] S. Grimme, Semiempirical GGA-type density functional constructed with a long-range dispersion correction, J. Comput. Chem. **27**, 1787 (2006).

[38] I. Popov, G. Seifert, and D. Tománek, Designing Electrical Contacts to MoS_2 Monolayers: A Computational Study, Phys. Rev. Lett. **108**, 156802 (2012).

[39] See Supplemental Material at http://link.aps.org/supplemental/10.1103/PhysRevB.96.205423 for (1) DFT results for bilayer metal/bilayer MoS_2 system, (2) XPS analysis and estimated upward shift of Fermi level from DFT calculation, (3) estimation of image force induced barrier lowering, (4) extraction of barrier height with $\alpha_{\text{eff}} = 1.5$, (5) coupled Poisson-Schrödinger equations, (6) contact resistance from a different set of TLMs, (7) contact resistance dependence on V_{ds}.

[40] S. Kallatt, G. Umesh, and K. Majumdar, Valley coherent hot carriers and thermal relaxation in monolayer transition metal dichalcogenides, J. Phys. Chem. Lett. **7**, 2032 (2016).

[41] B. Chakraborty, A. Bera, D. V. S. Muthu, S. Bhowmick, U. V. Waghmare, and A. K. Sood, Symmetry-dependent phonon renormalization in monolayer MoS_2 transistor, Phys. Rev. B **85**, 161403 (2012).

[42] S. M. Sze, *Physics of Semiconductor Devices*, 2nd ed. (Wiley, New York, 1981).

[43] M. Kleefstra and G. C. Herman, Influence of the image force on the band gap in semiconductors and insulators, J. Appl. Phys. **51**, 4923 (1980).

[44] A. Anwar, B. Nabet, J. Culp, and F. Castro, Effects of electron confinement on thermionic emission current in a modulation doped heterostructure, J. Appl. Phys. **85**, 2663 (1999).

[45] J. Bardeen, Tunnelling from a Many-Particle Point of View, Phys. Rev. Lett. **6**, 57 (1961).

[46] J. Tersoff and D. R. Hamann, Theory and Application for the Scanning Tunneling Microscope, Phys. Rev. Lett. **50**, 1998 (1983).

[47] Y. Kim, A. R. Kim, J. H. Yang, K. E. Chang, J.-D. Kwon, S. Y. Choi, J. Park, K. E. Lee, D.-H. Kim, S. M. Choi, K. H. Lee, B. H. Lee, M. G. Hahm, and B. Cho, Alloyed 2D metal–semiconductor heterojunctions: Origin of interface states reduction and Schottky barrier lowering, Nano Lett. **16**, 5928 (2016).

[48] S. Datta, *Quantum Transport: Atom to Transistor* (Cambridge University Press, Cambridge, UK, 2005).

[49] K. Majumdar and N. Bhat, Bandstructure effects in ultra-thin-body double-gate field effect transistor: A fullband analysis, J. Appl. Phys. **103**, 114503 (2008).